Check for updates

Water Practice & Technology

IWA PUBLISHING

© 2023 The Authors

Water Practice & Technology Vol 18 No 6, 1317 doi: 10.2166/wpt.2023.089

Green synthesis of mesoporous 2D Mn_2O_3/rGO nanocomposite for effective removal of methyl orange

Amal H. Al-Bagawi

Chemistry Department, Faculty of Science, University of Ha'il, Hail, Kingdom Of Saudi Arabia
E-mail: amalelbagawi@gmail.com

AHA, 0000-0003-3175-5257

ABSTRACT

Green synthesis of di-manganese trioxide mesoporous structure (super nano porous) sheets (Mn_2O_3-rGO-NS), Graphene oxide nano sheets (GO) and Mn_2O_3-rGO-NS nano sheets composite (Mn_2O_3-rGO-NS) were prepared via Thermal decomposition, seconds timescale water electrolytic oxidation and sonication method respectively. The prepared samples were characterized via X-ray diffraction, FESEM, TEM , and FTIR. Average crystallite size was found about 38 and 26 nm for Mn_2O_3-NS and Mn_2O_3-rGO-NS, respectively. Mn_2O_3-rGO–NPs morphology reveal nano porous sheets within average 35 nm and 26 nm in pores diameter and thickness respectively. Mn_2O_3-NS act distributed on and between graphene sheets creating macro and nano pores. The obtained results showed that the characteristics of the α-Mn_2O_3-rGO-NS sheets were improved by the addition of rGO sheets. Methyl orange (MO) dye adsorption onto Mn_2O_3-rGO-NS composite was investigated at various adsorption parameters, including pH, adsorbent quantity, and time. It was discovered that the adsorption behavior complies with the intra-particle diffusion model and the Friedendlich isotherm. Methyl orange in aqueous media may be eliminated 99.3% by Mn_2O_3-rGO-NS composite.

Key words: α-Mn_2O_3, 2D nanostructure, manganese oxide, meso-porous, methyl orange dye removal, reduced graphene oxide composite

HIGHLIGHT

- Mesoporous graphene-based composite synthesis for dye removal from aqueous media with high efficiency and capacity. According to thermodynamics and kinetics adsorption is favorable, which opens up the possibility for further trials on various types of pollutant removal studies for the industry.

1. INTRODUCTION

The primary goal of modern nanotechnology research is the environmentally friendly synthesis of nanomaterials. Green synthesis of nanoparticles is a non-toxic, ecologically beneficial, clean, less expensive, and essentially novel method (Verma *et al.* 2019; Nakum & Bhattacharya 2022). Removal of dyes by adsorption-technology is a particularly important technique, because of its usability, simplicity, high efficiency, and scale-up over a wide range of concentrations (Kurniawan *et al.* 2012; Al Jebur & Alwan 2022). Nanomaterials are utilized for water treatment due to being eco-friendly, low-cost, high-performance materials that are well positioned for large-scale water treatment and elucidated in many field studies (Hashem 2014; Hairom *et al.* 2021; Jain *et al.* 2021). Metal oxides and their composites are commonly utilized in materials for pollution control and removal. Their various oxidation states, huge surfaces, and diverse electronic configurations give them these features (Liu *et al.* 2023).

Tuning synthesis in broad diversity of manganese oxides (such as MnO, MnO_2, Mn_2O_3, Mn_3O_4) morphology and type appear unique properties, and receive great scientific interest in various applications such as environmental control, batteries, magnetism, and pollution sensing applications (Ahmed *et al.* 2022a, 2022b). Mn_2O_3 (p-type semiconducting material) is regarded as likely candidate material as it is non-toxic, low-cost material, has superior structural flexibility, and is environmentally compatible (stable) (Vignesh *et al.* 2022). Various processes have been carried out to improve the properties of metal oxide nanoparticles by using different methods of

This is an Open Access article distributed under the terms of the Creative Commons Attribution Licence (CC BY 4.0), which permits copying, adaptation and redistribution, provided the original work is properly cited (http://creativecommons.org/licenses/by/4.0/).

Downloaded from http://iwaponline.com/wpt/article-pdf/18/6/1317/1244790/wpt0181317.pdf
by guest

preparation or trying to control the particle size or doping with other materials (Stankic *et al.* 2016; Pradeev Raj *et al.* 2018; Chavali & Nikolova 2019; Krstić 2021; Pan *et al.* 2021; Sharma *et al.* 2022). Mesoporous oxides have drawn considerable interest due to their attractive physical (surface area) and chemical (reactivity) properties, which promised enormous potential for their neutral effect on the environment and their capability for pollutant trapping (Zhang *et al.* 2020; Yu *et al.* 2022). Graphene has a hexagonal two-dimensional layer made up of sp^2 carbon atoms. It is well known for having a good electron acceptor, excellent charge transport, and a higher surface area, which has good mechanical, thermal, and electronic properties and can be utilized as nanosorbents, is typically composed of one or more atomically layer carbon atoms and it also has a special two-dimensional structure. The adsorption of dyes on a few-layered graphene nanosheets is made possible by Van der Waals forces and stacking interactions. Reduced graphene oxide nanosheets (rGO-NS) can improve metal oxide performance by first incorporating them into composite materials to change their chemical and physical properties (Sundriyal *et al.* 2018; Cong *et al.* 2021; Yeon *et al.* 2022). Strong intermolecular forces between adsorbates are provided by the broad electronic surfaces and high aspect ratios of both rGO-NS layers and single layers. Graphene performs admirably in terms of conductivity, flexibility, and chemical inertness. Lately, graphene-based material is of great scientific interest due to its superior mechanical characteristics, thermochemical stability and conductivity, which is predicted to have various uses (Li *et al.* 2010; Upadhyay *et al.* 2013; Kalaiselvi & Chandar 2021). Graphene oxide (GO) is a semiconductor material with a bandgap of 2.2 eV that can be decreased through reduction (Konale *et al.* 2020). The rGO has a bandgap in the range of 1–1.69 eV (Abid *et al.* 2018). This material previously was used to tune the optical, physico-chemical, adsorption efficiency, mechanical and promoted properties of metal oxides (Loh *et al.* 2010; Malefane *et al.* 2019; Ajala *et al.* 2022; Chi *et al.* 2022; Stefan *et al.* 2022). There are numerous methods for creating nanomaterials, the thermal decomposition process is being considered as a 'green method' that does not use or produce harmful chemicals or solvents (Dikshit *et al.* 2021). In addition, the procedure permits the preparation of a vast quantity of samples in a single batch compatible with ethics of COP 27 regulations (Nassar 2013; Nassar *et al.* 2013; Stanczyk 2022). In an effort to reduce the production of harmful wastes, this work created impacted nanosheets of Mn_2O_3-NS and Mn_2O_3-rGO with thickness less than 100 nm simply by thermal decomposition of metal-citric extract and sonication respectively. The composites were described and their adsorption activity was evaluated. There is not much information in the literature about the study of rGO impact on the structural and adsorption properties of Mn_2O_3. So, synthesis of Mn_2O_3-rGO-NS by the green method in two-dimensional morphology and the investigation of adsorption isotherm and kinetics of Mn_2O_3-rGO-NS are the main objectives of this work.

2. EXPERIMENTAL

2.1. Chemicals and reagents

All chemicals were used without any further purification. Manganese (II) acetate tetra hydrate (Acros, 99+ %), citrus peel was obtained from a local market in Hail Region, Saudi Arabia. The fruit peel was removed from the pulp. During this process, aluminum foil was used to protect the samples from light. Sodium hydroxide (Fisher chemical, $\geq$ 97%) graphite rods (99% extra pure) were obtained from LOBA CHEMIE, India. Hydrochloric acid (HCl) (37%), nitric acid (HNO_3), sodium hydroxide (NaOH) powder, sulfuric acid (H_2SO_4), potassium permanganate ($KMnO_4$) and standard Ni (II) solution were purchased from Sigma Aldrich, USA, while hydrogen peroxide (H_2O_2) and sodium nitrate ($NaNO_3$) were purchased from PIOCHEM, Egypt and ISO-CHEM, France, respectively.

2.2. Synthesis of dimanganese trioxide nanosheets (Mn_2O_3-NS)

For the green synthesis Mn_2O_3-rGO-NS mesoporous nanosheets, 8 mM of manganese (II) acetate tetra hydrate ($C_4H_{16}MnO_8$) was added to 20 mL of Milli Q water and pH was adjusted to 4 (acidic medium) to obtain a flat two-dimensional sheet is consistent with previous reports (Wahab *et al.* 2009; Nagyné-Kovács *et al.* 2020; Xie *et al.* 2022). Using M acetic acid and M NaOH solution for pH optimization. After that, 90 mL of as-prepared citric extract from citrus peels (Fernandes *et al.* 2022) was then added to $C_4H_{16}MnO_8$ mixture and kept under vigorous magnetic stirring for 5 h at 78–80 °C. The visual color change and precipitate (ppt) were formed. The resulting ppt was centrifuged at 10,000 rpm for 20 min and washed several times with Milli Q water. Finally, ppt powder was dried at 85 °C for 6 h then calcined at 700 °C for 2 h. A dark brown residue of Mn_2O_3-NS was formed.

Downloaded from http://iwaponline.com/wpt/article-pdf/18/6/1317/1244790/wpt0181317.pdf
by guest

2.3. Graphene oxide (GO) synthesis

The GO was synthesized using Green method via seconds timescale water electrolytic oxidation (Pei *et al.* 2018).

2.4. Synthesis of Mn_2O_3-rGO nanocomposites

Mn_2O_3-rGO nanocomposites were prepared via the sonication method (Mohammadi & Entezari 2018) by mixing the GO and Mn_2O_3- NS (1:4) in 100 mL DI water, then probe sonicated for 30 min in pulsed mode at 600 W (20 KHz high frequency). Finally, homogeneous solutions of the Mn_2O_3-rGO nanocomposite were obtained and dried in a vacuum oven at 100 °C for 10 h.

2.5. Batch adsorption experiments

The amount of Mn_2O_3-rGO-NS nanoparticles adsorption trials began with 0.1 g (100 mg) achieving 50% removal and increasing directly proportional to the quantity added reaching the maximum removal of 99.3% at 0.5 g (500 mg). pH varies from 3 to 9, and contact time is the time needed to reach the equilibrium between the adsorbent and dyes. In a time range of 0–120 minutes, the impact of contact time on the removal of the dye by Mn_2O_3-rGO-NS at pH 4, and the concentration of the dye were all studied using a batch technique. All experiments were performed in triplicate to ensure repeatability and accuracy.

2.5.1. Batch adsorption kinetics

Variable amounts of Mn_2O_3-rGO-NS were stirred into a known amount of MO-dye to study the reaction kinetic isotherms. Measurements were used to determine the moment equilibrium was reached. The mixture was centrifuged at 4,000 rpm. The dye was identified using a UV-visible spectrophotometer at 464 nm. The dye solution's pH was changed using 0.1N NaOH and 0.1N HCl. Kinetic models were used to determine the controlling mechanism of the adsorption process. Three major models, namely pseudo-first-order, pseudo-second-order, and intra-particle diffusion, were used to examine this adsorption. First Lagergren pseudo-first-order model of Revellame *et al.* (2020) is selected to fit the kinetic data, followed by pseudo-second-order model (Saha & Grappe 2017; Sahoo & Prelot 2020; Krstić 2021). The intra-particle diffusion equation is given as (Sousa *et al.* 2012; Kuroki *et al.* 2014; Pan *et al.* 2017):

$$q_t = k_i t^{0.5} + C.$$

where k_i (mg/g $min^{0.5}$) is the intra-particle diffusion rate constant, plots of q_t versus $t^{0.5}$ yield straight lines with intercept (C). The boundary layer thickness is described by the values of the intercept. The larger the intercept, the greater is the boundary layer effect (Lee *et al.* 2011; Balta *et al.* 2012; Anastopoulos *et al.* 2018). q_e and q_t are the sorption capacities per gram of sorbents (mg/g) at equilibrium and at time t (min), where k_1, k_2, and k_i are the rate constant of the pseudo-first-order, pseudo-second-order and intra particular respectively. For kinetic measurements, 1 L of 50 ppm solutions of MO-Dye were added with 400 mg of Mn_2O_3-rGO-NS at pH 4 and room temperature. By measuring the absorbance at 464 nm wavelength at various time intervals and using a calibration curve, the corresponding dye concentration (ppm) could then be calculated.

2.5.2. Bath adsorption isotherm

The adsorption isotherm, which is based on the homogeneity or heterogeneity of the adsorbent surface and the interaction between absorbed molecules, theoretically depicts the distribution of dye molecules between the adsorbent and liquid phase. To determine the best model for analysis and optimization of adsorption processes, the equilibrium adsorption data were examined using the most popular adsorption isotherms models, including Langmuir, Freundlich, and Temkin. Four hundred mg of Mn_2O_3-rGO-NS at pH 4 was added to a 1 L solution of various MO-Dye concentrations (10, 20, 30, 40, 50 and 60 ppm), to evaluate the adsorption isotherms.

2.5.2.1. Langmuir adsorption isotherm. Langmuir isotherm assumes that during the adsorption process the monolayer is formed at specific homogeneous sites on the surface of the adsorbent, without any interaction between adsorbate molecules The linear form of Langmuir adsorption isotherm is expressed as (Langmuir 1918):

$$\frac{C_e}{q_e} = \frac{1}{K_L q_{\max}} + \frac{C_e}{q_{\max}}$$

Downloaded from http://iwaponline.com/wpt/article-pdf/18/6/1317/1244790/wpt0181317.pdf
by guest

where C_e is the equilibrium concentration, q_{max} (mg/g) is the maximum adsorption capacity of the adsorbent corresponding to monolayer formation. KL is the Langmuir constant.

2.5.2.2. Freundlich adsorption isotherm. Freundlich isotherm offers an empirical isotherm that is used to represent multilayer adsorption and assumes that the adsorption occurs on a heterogeneous surface and layers.

The linear form of Freundlich isotherm is given by the following equation (Freundlich 1906, 1910):

$$(\ln q_e = \ln k_f + \frac{1}{n} \ln C_e)$$

where k_f is a Freundlich isotherm constant (mg/g), C_e is the equilibrium concentration of adsorbate (mg/L), q_e is the amount adsorbed per gram of the adsorbent at equilibrium (mg/g).

2.5.2.3. Temkin adsorption isotherm. The adsorption of heterogeneous surface energy systems (non-uniform distribution of sorption heat) is described by this Temkin isotherm, it is based on the supposition that the adsorption heat, a function of temperature, decreases linearly with coverage as a result of interactions between the adsorbent and the adsorbate. The Temkin isotherm's linear form can be represented as follows (Temkin & Pyzhev 1940; Johnson & Arnold 1995):

$$(q_e = B\ \ln A_T + B \ln C_e)$$

The B is constant which is equal to RT/bT. A_T (L/mg) and B_T (J/mol) are the Temkin constants. B_T is related to the heat of adsorption and A_T is the equilibrium binding constant corresponding to the maximum binding energy. R (8.314 J/mol K) is the universal gas constant in energy unit and T (K) is the absolute temperature. The values of A_T and B_T are calculated from the linear plots of q_e versus ln C_e.

2.6. Characterization techniques

The phase composition and crystal structure examined via the X-ray diffraction (XRD), model Malvern Panalytical Empyrean. The TEM images of the samples were determined via transmission electron microscope (TEM), model Joel-JEM-2100, operated at 200 kV. The FTIR spectra were collected using a FTIR spectrometer, model Vertex 70-Bruker, Germany (in the range of 400–4,000 cm^{-1} with a resolution of 4 cm^{-1}). The UV-vis absorption spectra of the samples were measured using a double beam spectrophotometer (Perkin Elmer Lambda 40).

3. RESULTS AND DISCUSSION

3.1. X-ray diffraction

Figure 1 shows the XRD pattern of the as-prepared graphene oxide, Mn_2O_3- NS and Mn_2O_3/rGO. In Figure 1, the diffraction pattern of the GO only peak at $2\theta = 1.11°$ indexed for (002) plane confirmed the efficiency of the oxidation reaction with an increase in the inter planar distance of the graphene nano-platelets and it would be clear on FESEM (Castro Neto *et al.* 2009; Arbuzov *et al.* 2013; Han *et al.* 2014; Stobinski *et al.* 2014; Gascho *et al.* 2019). Mn_2O_3-NS pattern profiles indicated the seven characteristic diffraction peaks of the cubic α-Mn_2O_3 phase with reference code (JCPDS No. 01-081-9976). observed at 23.1, 32.9, 38.2, 45.1, 49.3, 55.2 and 65.7° which are assigned to (211), (222), (400), (332), (431), (440), and (622) planes with D-spacing 1.41, 1.66, 1.84, 2.00, 2.30, 2.70 and 3.80 respectively (Najjar *et al.* 2019; Mokkath *et al.* 2021). All diffraction peaks intensities of Mn_2O_3-NS were decreased after probe-sonication processing and composite forming, indicating that the face-to-face stacking is present because of the formation of Mn_2O_3-rGO on both sides of the rGO sheets and it would be clear in FESEM images. Previous investigations have shown the disappearance of rGO diffraction peaks for regular stacking exfoliated graphene oxides (Jung *et al.* 2020) and this is a good indication of rigid bonding.

The addition of rGO to the Mn2O3-rGO matrix broadens the major peaks while lowering their intensities, indicating that particle size has changed. This broadening is caused by the finite size of the particles and the microstrain formed in the crystal structure. To confirm this data, the average crystallite size ($D_{(222)}$) for the maximum

Downloaded from http://iwaponline.com/wpt/article-pdf/18/6/1317/1244790/wpt0181317.pdf
by guest

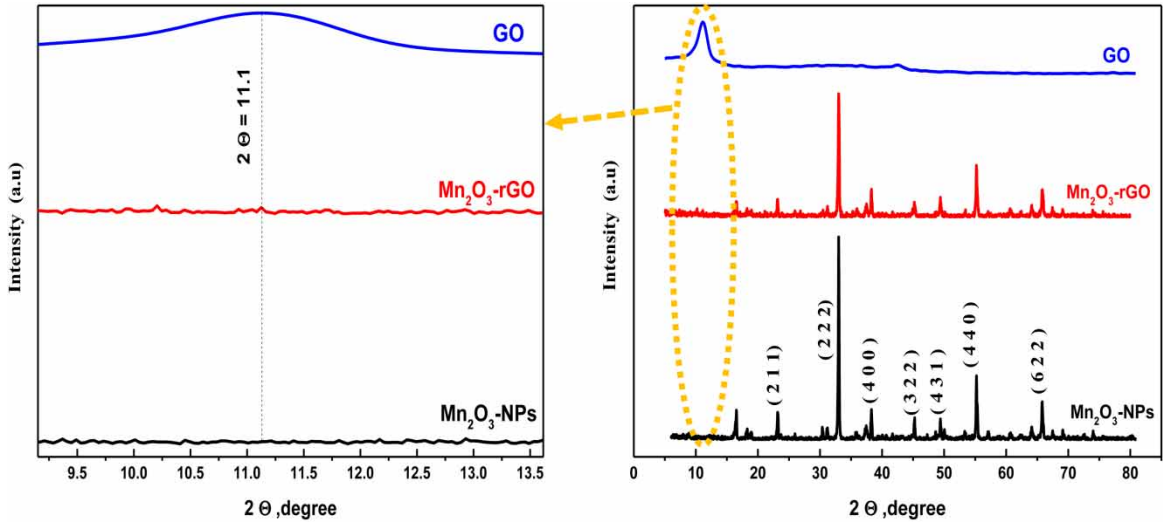

Figure 1 | XRD pattern of graphene oxide (GO), Mn_2O_3-rGO and Mn_2O_3-rGO nanoparticles.

peak with (222) plane can be calculated via the Scherer's equation (Nassar 2013):

$$D_{(222)} = \frac{0.9\ \lambda}{\beta_{(222)} \cos\theta} \tag{1}$$

where β is the full width at half maximum (FWHM) for (222) plane, θ is the Bragg's angle, and λ is the wavelength of X-ray. The average crystallite size was found to be about 38 and 26 nm for Mn2O3-rGO and Mn_2O_3-rGO composites, respectively.

One of the main reasons for the strain growth inside the crystal structure is the existence of defects inside the matrix. These defects clearly appeared in the existence of short peaks and disappeared in the presence of rGO sheets in the matrix as shown in the XRD pattern. The micro-strain (ε) and the dislocation density (δ) are important parameters that can be investigated from the XRD pattern via the following relations (Vignesh *et al.* 2022):

$$\varepsilon_{(222)} = \frac{\beta_{(222)}}{4\tan\theta} \tag{2}$$

$$\delta_{(222)} = \frac{1}{D^2_{(222)}} \tag{3}$$

The ε and δ values are calculated and tabulated in Table 1.

Table 1 | Crystallite size (D), micro-strain (ε), and dislocation density (δ)

Sample	$D_{(222)}$ (nm)	$\varepsilon_{(222)}$, $\times 10^{-3}$	$\delta_{(222)}$, $\times 10^{14}$ (m^{-2})
Mn_2O_3	56	2.3	3.2
Mn_2O_3-rGO	43	3	5.5

As shown, ε and δ values were increased when rGO was inserted in the matrix. This result confirms the compression of the material and consequently the particle size decreases as well (Vignesh *et al.* 2022).

3.2. FESEM-TEM analysis

In order to accurately understand the morphology and the internal structure of the Mn_2O_3-NS, graphene oxide and Mn_2O_3-rGO-NS composite, FE-SEM at different magnifications and TEM were performed. The Mn_2O_3-rGO The nano flakes' surface structure was tightly packed and uniformly stacked against one another, with meso pores clearly visible at the top layers (Figure 2(a)–2(c)). Deep scanning by TEM revealed pores diameter within 33 nm and flakes thickness within 26 nm (Figure 2(d)–2(e)). Figure 2(f) of SAED depicts manganese oxide in a

Downloaded from http://iwaponline.com/wpt/article-pdf/18/6/1317/1244790/wpt0181317.pdf
by guest

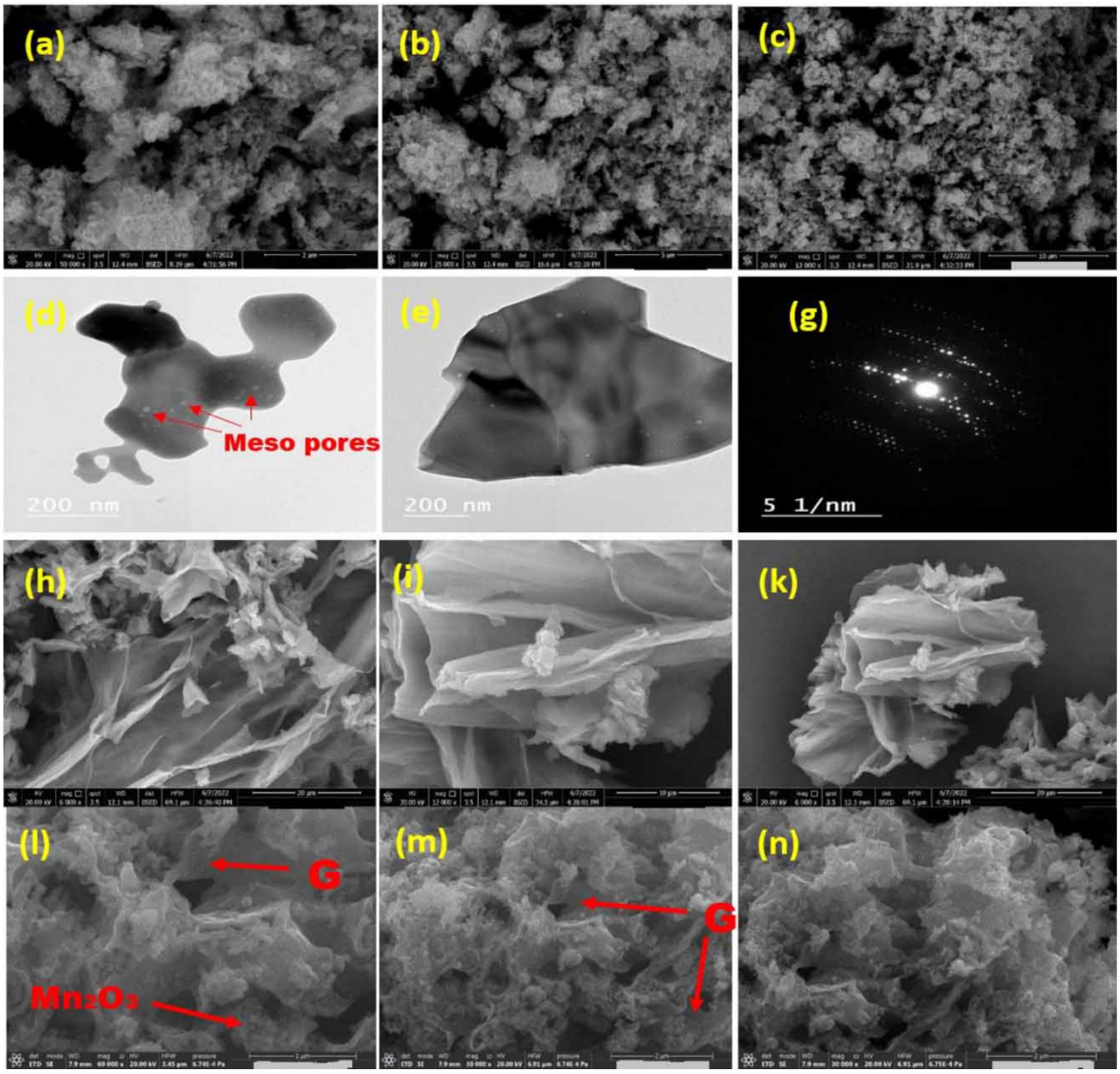

Figure 2 | FESM images of (a, b, e) Mn_2O_3-NS, TEM images (c, d, g) Mn_2O_3-NS, FESEM images (h,i,k) of graphene nanosheets and FESEM (l,m,n) Mn_2O_3/G composite.

polycrystalline structure that exists in 2D-shape (Tsuji & Fujita 2001). A wrinkled sheet-like microstructural structure of synthesized graphene is also observed in Figure 2(h) –2(k) FESEM, with the average length within 10 μm. Stacking composites were created after sonication in Figures 2(l) –2(n) show graphene layers inserted between well-spaced and sequenced Mn_2O_3 flakes. As high-energy projectiles struck graphite clusters, nanoporous Mn_2O_3-rGO micro-clusters with higher density than graphene agglomerations exfoliated them to graphene, improving uniformity and mixing of the composites. Collapsing on wrinkled graphene layers created new pores in the composite grain at the micro and nanoscales. Nanoparticle aggregates are primarily caused by the combination of tiny particles with high surface energy.

3.3. FT-IR analysis

In the wavenumber range between 200 and 3,600 cm^{-1}, Figure 3 displays the FTIR spectra of Mn_2O_3-NS and those that also contain reduced graphene oxide (RGO). The characteristic Mn-O stretching mode of Mn_2O_3-NS is attributed to the FTIR pattern's peaks located at 516, 576, and 670 cm^{-1}. The bands in the range 1,400–1,640 cm^{-1} comprise a characteristic stretching vibration mode of water (H_2O) absorbed by the samples. The peaks appearing at 1,710 and 1,014 cm^{-1} are characteristic for the C = C and C-O alkoxide of the rGO, especially the C = C frequency which appears clearly on the composite accompanied by slight red-shift (1,600 cm^{-1}). The observed peaks at 1,049 and 1,090 cm^{-1}, corresponding to C–H vibration, are due to the

Downloaded from http://iwaponline.com/wpt/article-pdf/18/6/1317/1244790/wpt0181317.pdf
by guest

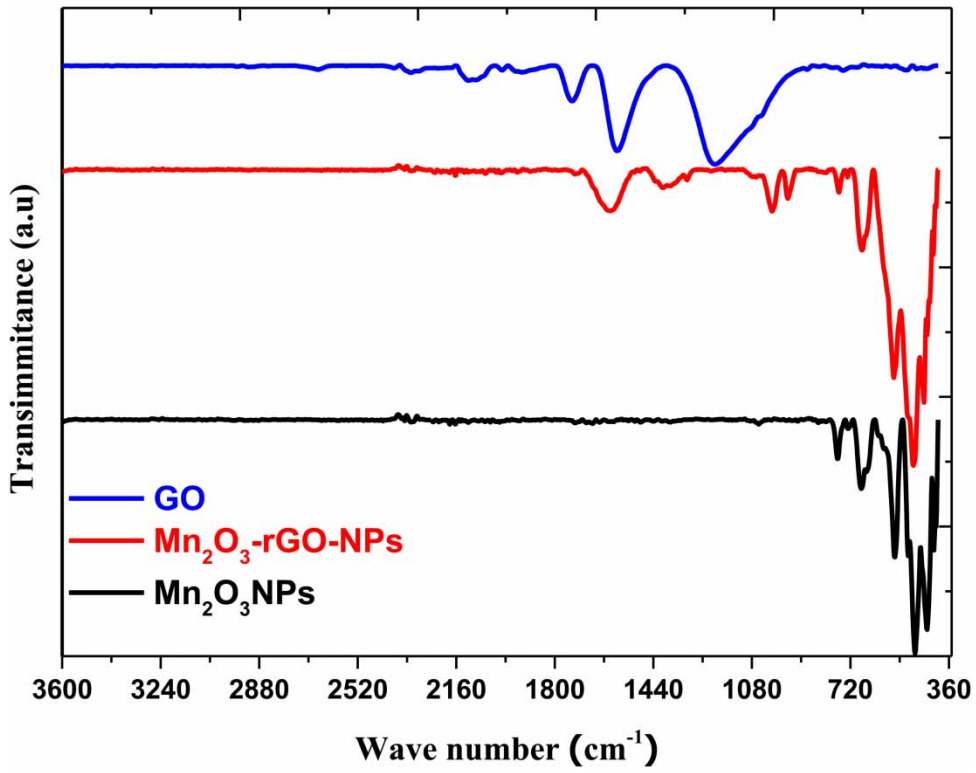

Figure 3 | FTIR of Mn_2O_3, Mn_2O_3-rGO, and GO.

preparation residuals. When RGO was added, no additional peaks were noticed. The absorbance of OH and C = O in FT-IR chart of rGO deceased in comparison to absorbance of the GO chart due to reduction via sonication.

3.4. Adsorption study

Batch adsorption was studied along with other parameters such as pH, Mn_2O_3-NS concentration, Methyl Orange starting concentration, and contact time. While maintaining all other variables constant throughout the study (temperature = 25 °C and stirring power = 300 rpm), the study hinges on modifying the parameter to determine its impact on the adsorption process.

3.4.1. Effects of pH on adsorption

The trials were carried out between pH values of 3 and 9, as shown in Figure 4. At pH 4, the highest adsorption (99.3%) was attained. The positively charged Mn_2O_3-rGO composite will be adsorbed with the sulfonate group of MO-dye at pH 4. The observation that the removal process slows down as pH rises may be explained by the fact that, while there will be fewer positively charged sites on Mn_2O_3-rGO -NS at higher pH, there will also be a rise in negatively charged sites, which will not favor the adsorption of the MO-dye due to electrostatic repulsion (Coruh *et al.* 2011; Jahan *et al.* 2022). In particular, the MO-dye molecules will face competition with the newly formed Mn_2O_3-rGO hydroxyl in the process of adhering to active sites. This suggests that water will accumulate in layers on top of metal oxide sheets. Surface OH is created when Mn^{2+} forms hydroxo complexes with OH groups from H_2O molecules on the top layer of Mn_2O_3-rGO surfaces. This interaction will mostly induce Mn-OH to make up the surface layer. Because they are not chemically or physically comparable, the surface hydroxo groups (OH) will dissociate and produce negatively charged O (Bhatnagar *et al.* 2010; Wang *et al.* 2020; Nizam *et al.* 2021). MO-dye at pH 4 will be positively charged and will be adsorbed to the negatively charged surface of Mn_2O_3-rGO-NS. In addition, the possibility of hydrogen bond formation between dye and rGO substrate and occlusion of the dye into Mn_2O_3-rGO-NS is supported by the presence of meso-structures on Mn_2O_3-rGO-NS as indicated from FESEM images.

3.4.2. Effect of weight of Mn_2O_3-rGO nanoparticles

To evaluate the impact of Mn_2O_3 -rGO quantities and the removal of MO, interval amounts of 100–500 mg of Mn_2O_3-rGO at 25 °C and pH 4 were added to 1 L (50 ppm) of MO-dye solutions. The outcomes demonstrate

Downloaded from http://iwaponline.com/wpt/article-pdf/18/6/1317/1244790/wpt0181317.pdf
by guest

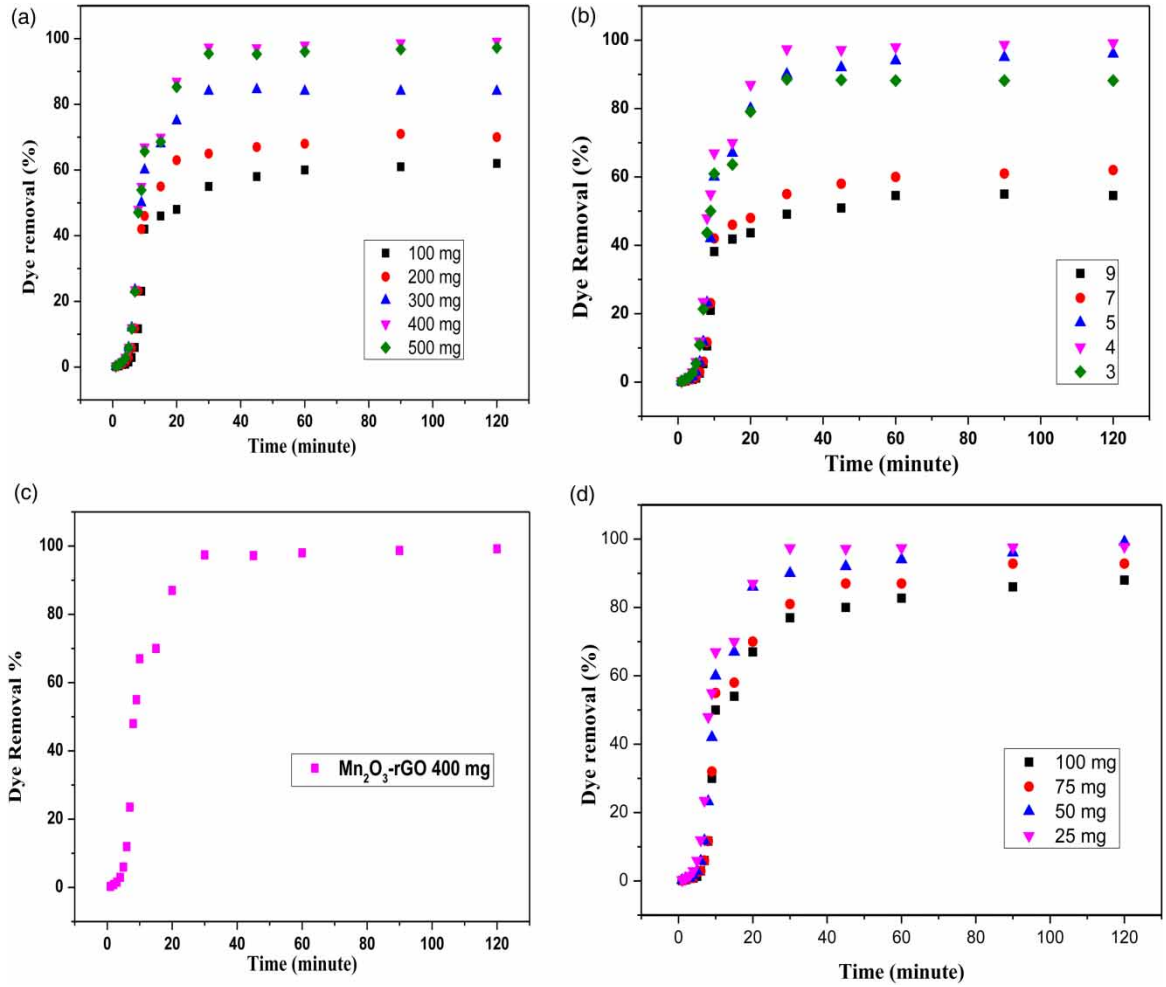

Figure 4 | Relation between percent (%) of removed dye and Mn_2O_3-rGO –NS at diverse parameters, (a) adsorbent (Mn_2O_3-rGO-NS) weight (mg), (b) pH, (c) Contact Time and (d) different concentration of MO-dye.

that the Mn_2O_3-rGO-NS concentration rises, the elimination of MO-dye also rises; 99.3% of the maximum removal was attained with 0.4 g of Mn_2O_3. The abundance of low energy active sites contributes to the gradual increase in removal efficiency. The remaining active sites will then have more energy, which will lead to a decrease in adsorption capacity that is associated to the development of stacking layers and unequal distribution (Chen *et al.* 2023).

3.4.3. Effect of contact time

In a time range of 0–120 minutes, the impact of contact time on the removal of the dye by Mn_2O_3-rGO-NS at pH 4 was examined. Figure 4(c) of the results showed that removal rises with increasing time until it achieves constant adsorption after 40 min. The active sites on the surface of Mn_2O_3-rGO-NS are predicted to become saturated with the dye after 40 minutes, at which point there will be no active sites left for adsorption.

3.4.4. Effect of the initial concentration of dye

A batch method of dye concentrations (30, 50, 60, 70, 80, and 90 mg/L) was used to study adsorption isotherms and influence of initial on the removal efficiency. The remaining dye in solution can be measured spectrophotometrically at 464 nm. The influence of initial dye concentrations concentration on the removal efficiency of MO-dye was studied as shown in Figure 3(d) using the same weight of Mn_2O_3-rGO-NS (0.4 gm) at pH 4, keeping all other factors constant. As can be seen in Figure 3(d), the percentage removal of the dye was found to decrease with the increase in initial dye concentration up to 50 mg/L. This suggests that according to active size availability, adsorption energy need, and competition between solvent and dye molecules with adsorbate and one another, saturation occurs.

Downloaded from http://iwaponline.com/wpt/article-pdf/18/6/1317/1244790/wpt0181317.pdf
by guest

3.4.5. Adsorption kinetics

Parameters were calculated from Figure 5(a)–5(c), the rate constants (k_1, k_2, k_i, and q_e) and related R^2 coefficient values are presented in Table 2. The correlation coefficients (R^2) are used to describe the applicability of the adsorption kinetics model. The R^2 values for the pseudo-first-order model are the lowest among the used models. Moreover, the value of q_e (experimental) differs significantly from that of q_e (calculated), which indicates the pseudo-first-order model does not work for the adsorption of MO-dye by Mn_2O_3-rGO-NS. However, the R^2 values for the pseudo-second-order kinetic model are higher than 0.91, but the values of (exp) are still different from that of (cal), but more closely than that of the first-order model, which indicates the pseudo-second-order (chemisorption) may be used to explain the adsorption of dye but not the only one. As the above two models cannot give definite mechanisms (Weber & Morris 1962; Crank 1975; McKay *et al.* 1987). Figure 5(c) shows tje relation between adsorbate species which moving from solution matrix to internal pores and gaps of nanoparticles (McKay *et al.* 1982, 1984; Sundaram *et al.* 2011). According to the results obtained in Table 2, we note that the intra-particle diffusion model is the most reliable way to explain this adsorption, since it has the best correlation coefficient ($R^2 = 0.99$). As shown in Figure 5, the fact that the straight lines do not pass through the origin

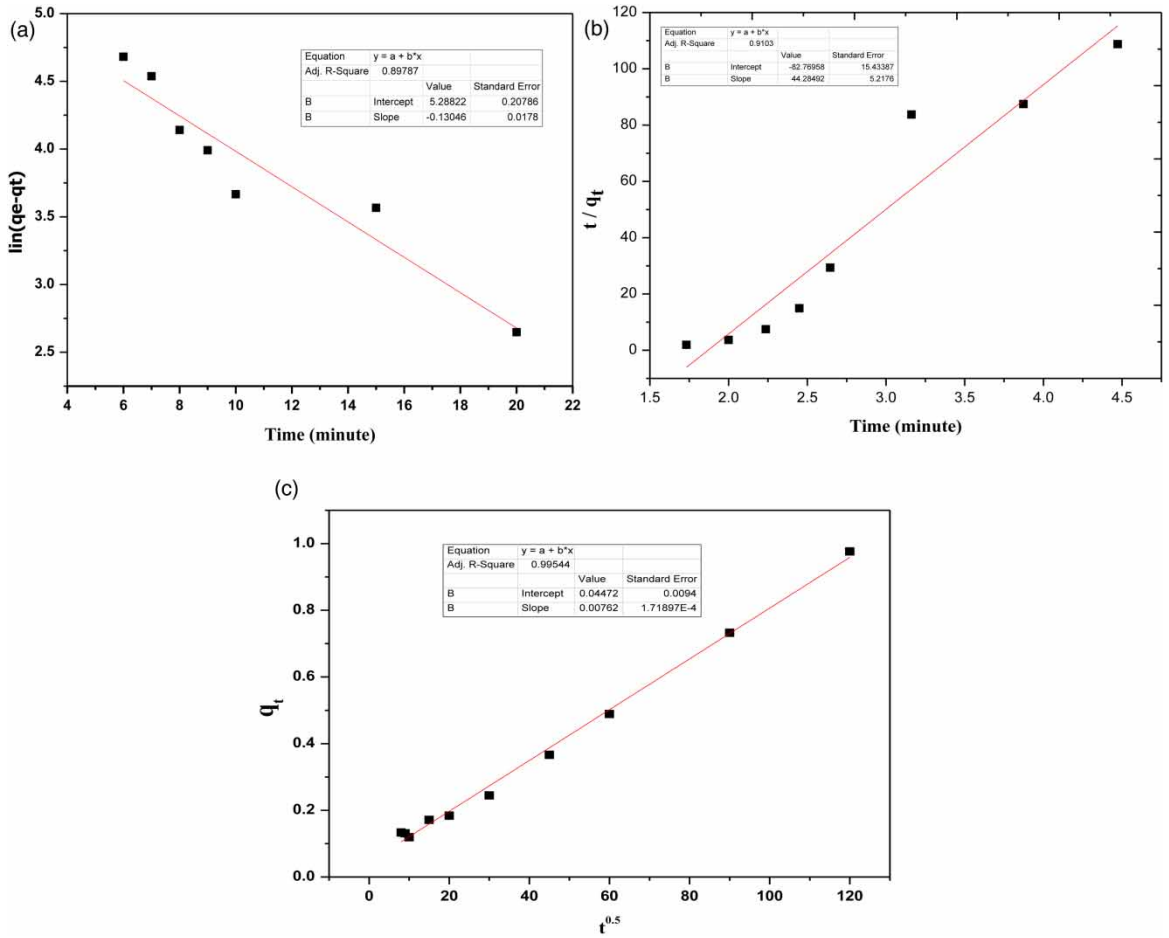

Figure 5 | Kinetic models of MO-dye adsorption on Mn_2O_3-rGO-NS. (a) The pseudo-first-order model, (b) The pseudo-second-order model, (c) The intra-particle diffusion model.

Table 2 | Experimental and calculated parameters of kinetics models of adsorption of MO-dyes

	Pseudo first order			Pseudo second order			Intra-particle diffusion		
q_e (exp)	q_e (cal.)	k_1	R^2	q_e (cal.)	k_2	R^2	C	k_1	R^2
99.3	215.17	0.194	0.89	181.34	2.7×10^{-4}	0.913	–17.03	22.2	0.99

Downloaded from http://iwaponline.com/wpt/article-pdf/18/6/1317/1244790/wpt0181317.pdf
by guest

shows that various kinetic models, which may all be active at the same time, may restrict the rate of adsorption and that intra-particle diffusion is not the only rate-limiting process. These findings support the existence of an intra-particle diffusion mechanism as well as surface adsorption (chemisorption) when it comes to the removal of MO-dye by Mn_2O_3-rGO-NS.

3.4.6. Adsorption isotherm

The values of the acquired parameters from the application to the experimental data obtained in the current investigation are shown in Figure 6(a)–6(c) of three models, which are the Freundlich, Langmuir, and Temkin models, respectively. The experimental results were found to fit the Freundlich isotherm model with a regression coefficient R^2 (0.98) and fit the Langmuir isotherm model with a lower regression coefficient R^2 (0.966), while they exhibit a poor-fitting with Temkin models R^2 (0.86). It is obvious from the data depicted that the Freundlich and Langmiur models better described the adsorption process than the Temkin model. The Freundlich model shows that maximum theoretical adsorption capacity is 210 mg/g, which is considered a high value in comparison to other adsorption capacities in published works (38.6 mg/g) (Chakrabarti *et al.* 2009) and 22.2 mg/g (Abdullah *et al.* 2021).

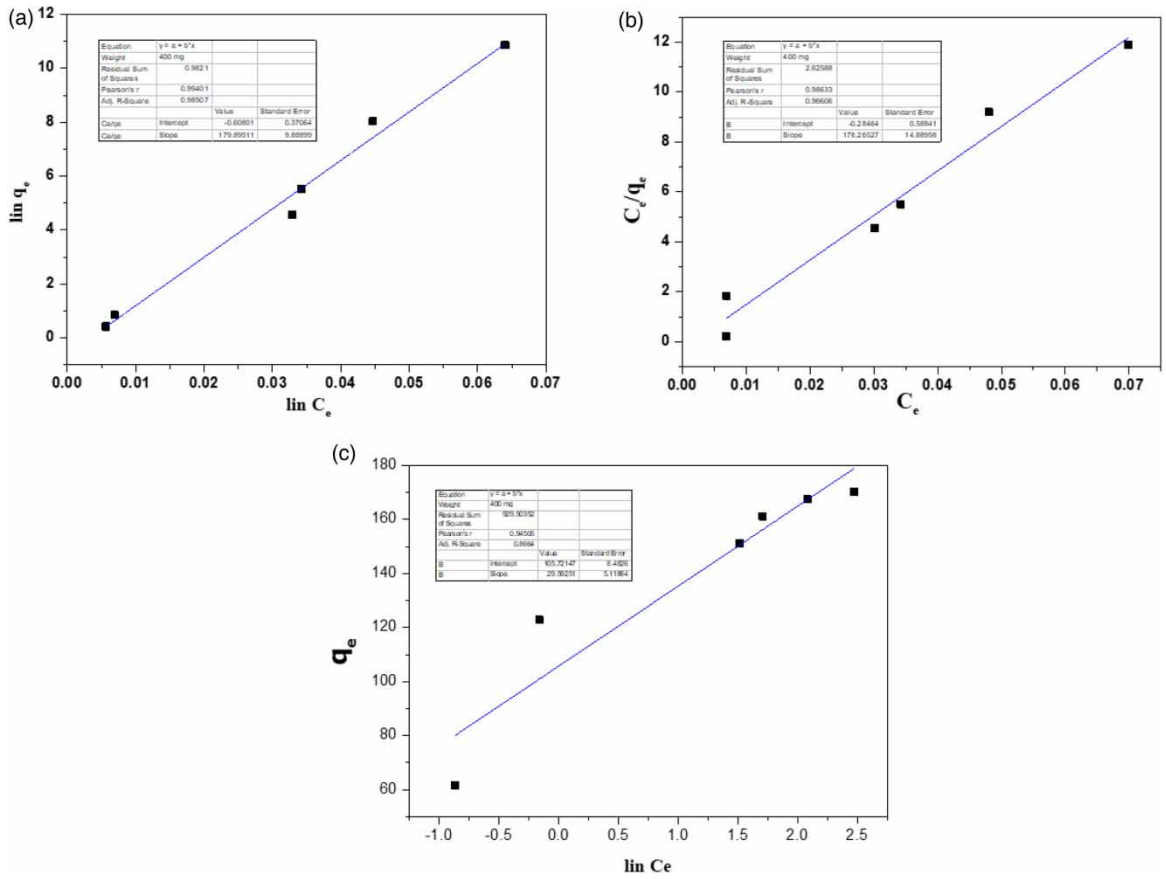

Figure 6 | Adsorption isotherm for MO-dyes over Mn2O3-rGO-NS. (a) Freundlich isotherm, (b) Langmuir isotherm, (c) Temkin isotherm.

4. CONCLUSIONS

This work opens a green synthesis gate for super nanoporous benign metal oxide (mesoporous structure of α-Mn_2O_3) with a thickness of less than 26 nm and graphene sheets using thermal decomposition of metal-citrus peels extracts complex and second timescale electrolytic oxidation respectively. Following that, a composite was formed via utilizing ultrasonic radiation. The obtained results showed that the characteristics of the Mn2O3-rGO-NS sheets were improved by the addition of rGO sheets. In comparison to the literature, Mn_2O_3-rGO-NS adsorption capacity exhibits a high adsorption capacity of 210 mg/g to MO dye when compared to the

Downloaded from http://iwaponline.com/wpt/article-pdf/18/6/1317/1244790/wpt0181317.pdf
by guest

literature at various adsorption parameters, including pH, adsorbent quantity, and time. It was discovered that the adsorption behavior complies with the intra-particle diffusion model and the Freundlich isotherm and the Langmuir isotherm model with a lower regression coefficient. This technique exhibits good practice for the synthesis of eco-friendly composite materials for the large-scale removal of dye from aqueous systems.

FUNDING

No funding for this research.

DATA AVAILABILITY STATEMENT

All relevant data are included in the paper or its Supplementary Information.

CONFLICT OF INTEREST

The authors declare there is no conflict.

REFERENCES

Abdullah, T. A., Rasheed, R. T., Juzsakova, T., Al-Jammal, N., Mallah, M. A., Cuong, L. P., Salman, A. D., Domokos, E., Ali, Z. & Cretescu, I. 2021 Preparation and characterization of MnO_2-based nanoparticles at different annealing temperatures and their application in dye removal from water. *International Journal of Environmental Science and Technology* **18**(6), 1499–1512. doi:10.1007/S13762-020-02956-X.

Abid, Sehrawat, P., Islam, S. S., Mishra, P. & Ahmad, S. 2018 Reduced graphene oxide (rGO) based wideband optical sensor and the role of temperature, defect states and quantum efficiency. *Scientific Reports* **8**(1). doi:10.1038/S41598-018-21686-2.

Ahmed, I., Rehman, W., Mir, S., Somaily, H. H., Khalid, M. & Numan, A. 2022a Graphene oxide sheets wrapped with poly (aniline-co-melamine) nanofibers furnished with SNO_2 nanoparticles for electrochemical energy storage. *Journal of Materials Research* **2022**, 1–17. doi:10.1557/S43578-022-00718-8.

Ahmed, S. F., Mofijur, M., Rafa, N., Chowdhury, A. T., Chowdhury, S., Nahrin, M., Islam, A. B. M. S. & Ong, H. C. 2022b Green approaches in synthesising nanomaterials for environmental nanobioremediation: technological advancements, applications, benefits and challenges. *Environmental Research* **204**, 111967. doi:10.1016/J.ENVRES.2021.111967.

Ajala, O. J., Tijani, J. O., Bankole, M. T. & Abdulkareem, A. S. 2022 A critical review on graphene oxide nanostructured material: properties, synthesis, characterization and application in water and wastewater treatment. *Environmental Nanotechnology, Monitoring & Management* **18**, 100673. doi:10.1016/J.ENMM.2022.100673.

Al Jebur, L. A. & Alwan, L. H. 2022 Development of nano-activated carbon and apply it for dyes removal from water. *Water Practice and Technology* **17**(1), 297–310. doi:10.2166/WPT.2021.105.

Anastopoulos, I., Hosseini-Bandegharaei, A., Fu, J., Mitropoulos, A. C. & Kyzas, G. Z. 2018 Use of nanoparticles for dye adsorption: review. *Journal of Dispersion Science and Technology* **39**(6). doi:10.1080/01932691.2017.1398661.

Arbuzov, A. A., Muradyan, V. E. & Tarasov, B. P. 2013 Synthesis of graphenelike materials by graphite oxide reduction. *Russian Chemical Bulletin* **62**(9), 1962–1966. doi:10.1007/S11172-013-0284-X.

Balta, S., Sotto, A., Luis, P., Benea, L., Van der Bruggen, B. & Kim, J. 2012 A new outlook on membrane enhancement with nanoparticles: the alternative of ZnO. *Journal of Membrane Science* **389**(1), 155–161. doi:10.1016/j.memsci.2011.10.025.

Bhatnagar, A., Vilar, V. J. P., Botelho, C. M. S. & Boaventura, R. A. R. 2010 Coconut-based biosorbents for water treatment – a review of the recent literature. *Advances in Colloid and Interface Science* **160**(1–2), 1–15. doi:10.1016/j.cis.2010.06.011.

Castro Neto, A. H., Guinea, F., Peres, N. M. R., Novoselov, K. S. & Geim, A. K. 2009 The electronic properties of graphene. *Reviews of Modern Physics* **81**(1), 109–162. doi:10.1103/REVMODPHYS.81.109.

Chakrabarti, S., Dutta, B. K. & Apak, R. 2009 Active manganese oxide: a novel adsorbent for treatment of wastewater containing azo dye. *Water Science and Technology* **60**(12), 3017–3024. doi:10.2166/WST.2009.758.

Chavali, M. S. & Nikolova, M. P. 2019 Metal oxide nanoparticles and their applications in nanotechnology. *SN Applied Sciences* **1**(6), 607. doi:10.1007/S42452-019-0592-3.

Chen, Y., Fan, C., Li, X., Ren, J., Zhang, G., Xie, H., Liu, B. & Zhou, G. 2023 Preparation of carbon black-based porous carbon adsorbents and study of toluene adsorption properties. *Journal of Chemical Technology and Biotechnology* **98**(1), 117–128. doi:10.1002/JCTB.7220.

Chi, Z., Ju, S., Liu, X., Sun, F. & Zhu, Y. 2022 Graphene oxide supported sulfidated nano zero-valent iron (S-nZVI@GO) for antimony removal: the role of active oxygen species and reaction mechanism. *Chemosphere* **308**(Pt 1), 136–253. doi:10.1016/J.CHEMOSPHERE.2022.136253.

Cong, R., Park, H. H., Jo, M., Lee, H. & Lee, C. S. 2021 Synthesis and electrochemical performance of electrostatic self-assembled nano-silicon@N-doped reduced graphene oxide/carbon nanofibers composite as anode material for lithium-ion batteries. *Molecules* **26**, 4831. doi:10.3390/MOLECULES26164831.

Coruh, S., Geyikci, F. & Nuri Ergun, O. 2011 Adsorption of basic dye from wastewater using raw and activated red mud. *Environmental Technology* **32**(11), 1183–1193. doi:10.1080/09593330.2010.529946.

Crank, J. 1975 *Mathematics of Diffusion*. Clarendon Press, Cambridge, UK.

Downloaded from http://iwaponline.com/wpt/article-pdf/18/6/1317/1244790/wpt0181317.pdf
by guest

Dikshit, P. K., Kumar, J., Das, A. K., Sadhu, S., Sharma, S., Singh, S., Gupta, P. K. & Kim, B. S. 2021 Green synthesis of metallic nanoparticles: applications and limitations. *Catalysts* **11**, 902. doi:10.3390/CATAL11080902.

Fernandes, F. A., Heleno, S. A., Pinela, J., Carocho, M., Prieto, M. A., Ferreira, I. C. F. R. & Barros, L. 2022 Recovery of citric acid from citrus peels: ultrasound-assisted extraction optimized by response surface methodology. *Chemosensors* **10** (7), 257. doi:10.3390/CHEMOSENSORS10070257.

Freundlich, H. 1906 Uber die adsorption in losungen [Over the adsorption in solution]. *Journal of Physical Chemistry* **4**(11), 88–105.

Freundlich, H. 1910 Die bedeutung der adsorption bei der fällung der suspensionskolloide [The importance of adsorption in the precipitation of suspension colloids]. *Zeitschrift für Chemie und Industrie der Kolloide*. doi:10.1007/BF01510141.

Gascho, J. L. S., Costa, S. F., Recco, A. A. C. & Pezzin, S. H. 2019 Graphene oxide films obtained by vacuum filtration: x-ray diffraction evidence of crystalline reorganization. *Journal of Nanomaterials* **2019**, 124–149. doi:10.1155/2019/5963148.

Hairom, N. H. H., Soon, C. F., Mohamed, R. M. S. R. & Morsin, M. 2021 A review of nanotechnological applications to detect and control surface water pollution. *Environmental Technology and Innovation* **24**(3), 102032. doi:10.1016/j.eti.2021.102032.

Han, F., Yang, S., Jing, W., Jiang, K., Jiang, Z., Liu, H. & Li, L. 2014 A highly efficient synthetic process of graphene films with tunable optical properties. *Applied Surface Science* **314**, 71–77. doi:10.1016/J.APSUSC.2014.05.222.

Hashem, E. A. 2014 Nanotechnology in water treatment, case study, Egypt. *Journal of Economics and Devopment Studies* **2**(3), 243–259. doi:10.15640/JEDS.V2N3A18.

Jahan, N., Roy, H., Reaz, A. H., Arshi, S., Rahman, E., Firoz, S. H. & Islam, M. S. 2022 A comparative study on sorption behavior of graphene oxide and reduced graphene oxide towards methylene blue. *Case Studies in Chemical and Environmental Engineering* **6**, 100239. doi:10.1016/J.CSCEE.2022.100239.

Jain, K., Patel, A. S., Pardhi, V. P. & Flora, S. J. S. 2021 Nanotechnology in wastewater management: a new paradigm towards wastewater treatment. *Molecules* **26**(6), 1797. doi:10.3390/MOLECULES26061797.

Johnson, R. D. & Arnold, F. H. 1995 The Temkin isotherm describes heterogeneous protein adsorption. *Biochimica et Biophysica Acta* **1247**(2), 293–297. doi:10.1016/0167-4838(95)00006-G.

Jung, J., Jeong, J. R., Lee, J., Lee, S. H., Kim, S. Y., Kim, M. J., Nah, J. & Lee, M. H. 2020 *In situ* formation of graphene/metal oxide composites for high-energy microsupercapacitors. *NPG Asia Materials* **12**(1), 1–9. doi:10.1038/s41427-020-0230-y.

Kalaiselvi, C. & Chandar, N. K. 2021 Graphene decorated long single crystalline Mn2O3 nanorods: facile synthesis and visible light photocatalyst. *Diamond and Related Materials* **120**, 108703. doi:10.1016/J.DIAMOND.2021.108703.

Konale, R. A., Mahale, N. K. & Ingle, S. T. 2020 Nano-zeolite-graphene oxide composite for calcium hardness removal: isotherm and kinetic study. *Water Practice and Technology* **15**(4), 1011–1031. doi:10.2166/WPT.2020.079.

Krstić, V., 2021 Role of zeolite adsorbent in water treatment. In: *Handbook of Nanomaterials for Wastewater Treatment* (Bhanvase, B. A., Sonawane, S. H., Pawade, V. B. & Pandit, A. B., eds). Elsevier, Amsterdam, The Netherlands, pp. 417–481. doi:10.1016/B978-0-12-821496-1.00024-6.

Kurniawan, T. A., Sillanpää, M. E. T. & Sillanpää, M. 2012 Nanoadsorbents for remediation of aquatic environment: local and practical solutions for global water pollution problems. *Critical Reviews in Environmental Science and Technology* **42**(12), 1233–1295. doi:10.1080/10643389.2011.556553.

Kuroki, V., Bosco, G. E., Fadini, P. S., Mozeto, A. A., Cestari, A. R. & Carvalho, W. A. 2014 Use of a La (III)-modified bentonite for effective phosphate removal from aqueous media. *Journal of Hazardous Materials* **274**, 124–131. doi:10.1016/J.JHAZMAT.2014.03.023.

Langmuir, I. 1918 The adsorption of gases on plane surfaces of glass, mica and platinum. *Journal of the American Chemical Society* **40**(9), 1361–1403. doi:10.1021/ja02242a004.

Lee, J. E., Lee, N., Kim, T., Kim, J. & Hyeon, T. 2011 Multifunctional mesoporous silica nanocomposite nanoparticles for theranostic applications. *Accounts of Chemical Research* **44**(10), 893–902.

Li, Y., Lv, X., Lu, J. & Li, J. 2010 Preparation of sno2-nanocrystal/graphene-nanosheets composites and their lithium storage ability. *Journal of Physical Chemistry C* **114**(49), 21770–21774. doi:10.1021/JP1050047/SUPPL_FILE/JP1050047_SI_001.PDF.

Liu, X., Zhang, H. & Jing, G. 2023 Synthesis of cuprous oxide via ion exchange route for photocatalytic degradation of methylene blue. *Water Practice and Technology* **18**(2), 295–303. doi:10.2166/WPT.2023.005.

Loh, K. P., Qiaoliang, B., Goki, E. & Chhowalla, M. 2010 Graphene oxide as a chemically tunable platform for optical applications. *Nature Chemistry* **2**(12), 1015–1024. doi:10.1038/NCHEM.907.

Malefane, M. E., Ntsendwana, B., Mafa, P. J., Mabuba, N., Feleni, U. & Kuvarega, A. T. 2019 *In-situ* synthesis of tetraphenylporphyrin/tungsten (VI) oxide/reduced graphene oxide (TPP/WO3/RGO) nanocomposite for visible light photocatalytic degradation of Acid Blue 25. *ChemistrySelect* **4**(29), 8379–8389. doi:10.1002/SLCT.201901589.

Mckay, G. B., Blair, H. S. & Gardner, J. R. 1982 Adsorption of dyes on chitin. I. Equilibrium studies. *Journal of Applied Polymer Science* **27**(8), 3043–3057. doi:10.1002/app.1982.070270827.

McKay, G., Blair, H. S. & Gardner, J. R. 1984 The adsorption of dyes onto chitin in fixed bed columns and batch adsorbers. *Journal of Applied Polymer Science* **29**(5), 1499–1514. doi:10.1002/app.1984.070290504.

McKay, G., Otterburn, M. S. & Aga, J. A. 1987 Intraparticle diffusion process occurring during adsorption of dyestuffs. *Water, Air, and Soil Pollution* **36**(3), 381–390. doi:10.1007/BF00229680.

Downloaded from http://iwaponline.com/wpt/article-pdf/18/6/1317/1244790/wpt0181317.pdf
by guest

Mohammadi, Z. & Entezari, M. H. 2018 Sono-synthesis approach in uniform loading of ultrafine Ag nanoparticles on reduced graphene oxide nanosheets: an efficient catalyst for the reduction of 4-Nitrophenol. *Ultrasonics Sonochemistry* **44**, 1–13. doi:10.1016/J.ULTSONCH.2018.01.020.

Mokkath, J. H., Jahan, M., Tanaka, M., Tominaka, S. & Henzie, J. 2021 Temperature-dependent electronic structure of bixbyite α-Mn2O3 and the importance of a subtle structural change on oxygen electrocatalysis. *Science and Technology of Advanced Materials* **22**(1), 141–149. doi:10.1080/14686996.2020.1868949.

Nagyné-Kovács, T., Lukács, I. E., Szabó, A., Hernadi, K., Igricz, T., László, K., Szilágyi, I. M. & Pokol, G. 2020 Effect of pH in the hydrothermal preparation of monoclinic tungsten oxide. *Journal of Solid State Chemistry* **281**, 121044. doi:10.1016/J.JSSC.2019.121044.

Najjar, R., Awad, R. & Abdel-Gaber, A. M. 2019 Physical properties of Mn2O3 nanoparticles synthesized by co-precipitation method at different pH values. *Journal of Superconductivity and Novel Magnetism* **32**(4), 885–892. doi:10.1007/S10948-018-4765-X.

Nakum, J. & Bhattacharya, D. 2022 Various green nanomaterials used for wastewater and soil treatment: a mini-review. *Frontiers in Environmental Science* **9**, 420. doi:10.3389/FENVS.2021.724814/XML/NLM.

Nassar, M. Y. 2013 Size-controlled synthesis of CoCO3 and CO3O4 nanoparticles by free-surfactant hydrothermal method. *Materials Letters* **94**, 112–115. doi:10.1016/J.MATLET.2012.12.039.

Nassar, M. Y., Mohamed, T. Y. & Ahmed, I. S. 2013 One-pot solvothermal synthesis of novel cobalt salicylaldimine–urea complexes: a new approach to CO3O4 nanoparticles. *Journal of Molecular Structure* **1050**, 81–87. doi:10.1016/J.MOLSTRUC.2013.07.027.

Nizam, N. U. M., Hanafiah, M. M., Mahmoudi, E., Halim, A. A. & Mohammad, A. W. 2021 The removal of anionic and cationic dyes from an aqueous solution using biomass-based activated carbon. *Scientific Reports* **11**(1), 1–17. doi:10.1038/s41598-021-88084-z.

Pan, M., Lin, X., Xie, J. & Huang, X. 2017 Kinetic, equilibrium and thermodynamic studies for phosphate adsorption on aluminum hydroxide modified palygorskite nano-composites. *RSC Advances* **7**(8), 4492–4500. doi:10.1039/C6RA26802A.

Pan, S., Goudoulas, T. B., Jeevanandam, J., Tan, K. X., Chowdhury, S. & Danquah, M. K. 2021 Therapeutic applications of metal and metal-oxide nanoparticles: dermato-cosmetic perspectives. *Frontiers in Bioengineering and Biotechnology* **9**, 710. doi:10.3389/FBIOE.2021.724499/BIBTEX.

Pei, S., Wei, Q., Huang, K., Cheng, H. M. & Ren, W. 2018 Green synthesis of graphene oxide by seconds timescale water electrolytic oxidation. *Nature Communications* **9**(1), 1–9. doi:10.1038/s41467-017-02479-z.

Pradeev Raj, K., Sadaiyandi, K., Kennedy, A., Sagadevan, S., Chowdhury, Z. Z., Johan, M. R., Bin Aziz, F. A. & Rafique, R. F. 2018 Influence of Mg doping on ZnO nanoparticles for enhanced photocatalytic evaluation and antibacterial analysis. *Nanoscale Research Letters* **13**. doi:10.1186/S11671-018-2643-X.

Revellame, E. D., Fortela, D. L., Sharp, W., Hernandez, R. & Zappi, M. E. 2020 Adsorption kinetic modeling using pseudo-first order and pseudo-second order rate laws: a review. *Cleaner Engineering and Technology* **1**, 100032. doi:10.1016/J.CLET.2020.100032.

Saha, D. & Grappe, H. A. 2017 Adsorption properties of activated carbon fibers. *Activated Carbon Fiber and Textiles* **2017**, 143–165. doi:10.1016/B978-0-08-100660-3.00005-5.

Sahoo, T. R. & Prelot, B. 2020 Adsorption processes for the removal of contaminants from wastewater: the perspective role of nanomaterials and nanotechnology. *Nanomaterials for the Detection and Removal of Wastewater Pollutants* **1**, 161–222. doi:10.1016/B978-0-12-818489-9.00007-4.

Sharma, A., Saini, A. K., Kumar, N., Tejwan, N., Singh, T. A., Thakur, V. K. & Das, J. 2022 Methods of preparation of metal-doped and hybrid tungsten oxide nanoparticles for anticancer, antibacterial, and biosensing applications. *Surfaces and Interfaces* **28**. doi:10.1016/j.surfin.2021.101641.

Sousa, A. F., de Braga, T. P., Gomes, E. C. C., Valentini, A. & Longhinotti, E. 2012 Adsorption of phosphate using mesoporous spheres containing iron and aluminum oxide. *Chemical Engineering Journal* **210**, 143–149. doi:10.1016/J.CEJ.2012.08.080.

Stanczyk, A. 2022 Getting to COP27: bridging generational divide. *Development (Basingstoke)* **65**(1), 42–47. doi:10.1057/S41301-022-00335-2.

Stankic, S., Suman, S., Haque, F. & Vidic, J. 2016 Pure and multi metal oxide nanoparticles: synthesis, antibacterial and cytotoxic properties. *Journal of Nanobiotechnology* **14**(1), 1–20. doi:10.1186/S12951-016-0225-6.

Stefan, M., Leostean, C., Popa, A., Toloman, D., Perhaita, I., Cadis, A., Macavei, S. & Pana, O. 2022 Highly stable MWCNT-CoFe2O4 photocatalyst. EGA-FTIR coupling as efficient tool to illustrate the formation mechanism. *Journal of Alloys and Compounds* **928**, 167188. doi:10.1016/j.jallcom.2022.167188.

Stobinski, L., Lesiak, B., Malolepszy, A., Mazurkiewicz, M., Mierzwa, B., Zemek, J., Jiricek, P. & Bieloshapka, I. 2014 Graphene oxide and reduced graphene oxide studied by the XRD, TEM and electron spectroscopy methods. *Journal of Electron Spectroscopy and Related Phenomena* **195**, 145–154. doi:10.1016/J.ELSPEC.2014.07.003.

Sundaram, M. M., Kannan, N. & Rejinis, J. 2011 Removal of mixture of textile basic dyes using low cost Artocarpus heterophyllus seed carbon – a batch adsorption study. *Indian Journal of Environmental Protection.* **31**(7), 580–587.

Sundriyal, S., Sharma, M., Kaur, A., Mishra, S. & Deep, A. 2018 Improved electrochemical performance of rGO/TiO2 nanosheet composite based electrode for supercapacitor applications. *Journal of Materials Science: Materials in Electronics* **29**(15), 12754–12764. doi:10.1007/S10854-018-9393-5.

Temkin, M. J. & Pyzhev, V. 1940 Recent modification to Langmuir isotherms. *Acta Physiochem. USSR.* **12**, 217–225. doi:10.1016/0016-3287(93)90022-L.

Downloaded from http://iwaponline.com/wpt/article-pdf/18/6/1317/1244790/wpt0181317.pdf
by guest

Tsuji, M., Fujita, M., 2001 Polymers: electron microscopy and electron diffraction. In: *Encyclopedia of Materials: Science and Technology* (Buschow, K. H. J., Cahn, R., Flemings, M. C., Ilscner, B., Kramer, E. J., Mahajan, S. & Veyssiere, P., eds). Pergamon Press, Oxford, UK, pp. 7654–7664. doi:10.1016/B0-08-043152-6/01370-X.

Upadhyay, R. K., Soin, N. & Roy, S. S. 2013 Role of graphene/metal oxide composites as photocatalysts, adsorbents and disinfectants in water treatment: a review. *RSC Advances* **4**(8), 3823–3851. doi:10.1039/c3ra45013a.

Verma, A., Gautam, S. P., Bansal, K. K., Prabhakar, N. & Rosenholm, J. M. 2019 Green nanotechnology: advancement in phytoformulation research. *Medicines* **6**(1), 39. doi:10.3390/MEDICINES6010039.

Vignesh, R., Prabha, C. N., Sivakumar, R. & Sanjeeviraja, C. 2022 Optical constants, optical dispersion and group index parameters of Mn2O3 thin films. *Physica B: Condensed Matter* **624**, 413431. doi:10.1016/J.PHYSB.2021.413431.

Wahab, R., Kim, Y. S. & Shin, H. S. 2009 Synthesis, characterization and effect of pH variation on zinc oxide nanostructures. *Materials Transactions* **50**(8), 2092–2097. doi:10.2320/MATERTRANS.M2009099.

Wang, G., Li, G., Huan, Y., Hao, C. & Chen, W. 2020 Acrylic acid functionalized graphene oxide: high-efficient removal of cationic dyes from wastewater and exploration on adsorption mechanism. *Chemosphere* **261**, 127736. doi:10.1016/j.chemosphere.2020.127736.

Weber, W. J. & Morris, J. C. 1962 *Advances in Water Pollution Research*. Publ. Div., Pergamon Press, Cambridge, UK.

Xie, H., Li, Z., Cheng, L., Haidry, A. A., Tao, J., Xu, Y., Xu, K. & Ou, J. Z. 2022 Recent advances in the fabrication of 2D metal oxides. *iScience* **25**(1), 103598. doi:10.1016/J.ISCI.2021.103598.

Yeon, J. S., Gupta, N., Bhattacharya, P., Park, H. S., Yeon, J., Park, H., Gupta, N. & Bhattacharya, P. 2022 A new era of integrative ice frozen assembly into multiscale architecturing of energy materials. *Advanced Materials* **32**(19), 2112509. doi:10.1002/adfm.202112509.

Yu, H., Wang, W., Liu, M., Zhao, T., Lin, R., Hou, M., Kou, Y. & Chen, L. 2022 Versatile synthesis of dendritic mesoporous rare earth–based nanoparticles. *Science Advances* **8**(30). doi:10.1126/SCIADV.ABQ2356.

Zhang, W., Li, B., Sun, Y. G., Cao, A. M. & Wan, L. J. 2020 Spherical mesoporous metal oxides with tunable orientation enabled by growth kinetics control. *Journal of the American Chemical Society* **142**(42), 17897–17902. doi:10.1021/JACS.0C07938/SUPPL_FILE/JA0C07938_SI_001.PDF.

First received 30 October 2022; accepted in revised form 21 April 2023. Available online 30 May 2023

Downloaded from http://iwaponline.com/wpt/article-pdf/18/6/1317/1244790/wpt0181317.pdf
by guest